Elucidating the atomistic mechanisms underpinning plasticity in Li-Si nanostructures

Xin Yan,[1] Afif Gouissem,[1] Pradeep R. Guduru,[2] and Pradeep Sharma[1,3,4,*]
[1]*Department of Mechanical Engineering, University of Houston, Texas 77004, USA*
[2]*School of Engineering, Brown University, Providence, Rhode Island 02912, USA*
[3]*Department of Physics, University of Houston, Texas 77004, USA*
[4]*Material Science and Engineering Program, University of Houston, Texas 77004, USA*
(Received 20 July 2017; published 6 October 2017)

Amorphous lithium-silicon (a-Li-Si), especially in nanostructure form, is an attractive high-capacity anode material for next-generation Li-ion batteries. During cycles of charging and discharging, a-Li-Si undergoes substantive inelastic deformation and exhibits microcracking. The mechanical response to repeated lithiation-delithiation eventually results in the loss of electrical contact and consequent decrease of capacity, thus underscoring the importance of studying the plasticity of a-Li-Si nanostructures. In recent years, a variety of phenomenological continuum theories have been introduced that purport to model plasticity and the electro-chemo-mechanical behavior of a-Li-Si. Unfortunately, the micromechanisms and atomistic considerations underlying plasticity in Li-Si material are not yet fully understood and this impedes the development of physics-based constitutive models. Conventional molecular dynamics, although extensively used to study this material, is grossly inadequate to resolve this matter. As is well known, conventional molecular dynamics simulations can only address phenomena with characteristic time scales of (at most) a microsecond. Accordingly, in such simulations, the mechanical behavior is deduced under conditions of very high strain rates (usually, 10^8 s^{-1} or even higher). This limitation severely impacts a realistic assessment of rate-dependent effects. In this work, we attempt to circumvent the time-scale bottleneck of conventional molecular dynamics and provide novel insights into the mechanisms underpinning plastic deformation of Li-Si nanostructures. We utilize an approach that allows imposition of slow strain rates and involves the employment of a new and recently developed potential energy surface sampling method—the so-called autonomous basin climbing—to identify the local minima in the potential energy surface. Combined with other techniques, such as nudged elastic band, kinetic Monte Carlo and transition state theory, we assess the behavior of a-Li-Si nanostructures under tensile strain rates ranging from 10^3 to 10^8 s^{-1}. We find significant differences in the deformation behavior across the strain rates and discover that the well-known shear transformation zones (widely discussed in the context of amorphous materials) are formed by a "diffusionlike" process. We identify the *rotation* of the shear transformation zone as a key dissipation mechanism.

DOI: 10.1103/PhysRevMaterials.1.055401

I. INTRODUCTION

Rechargeable lithium-ion batteries find applications in portable electronics, electric vehicles, and many other contexts where a compact energy storage system is required [1–3]. Due to the critical role batteries are likely to play in the future energy storage needs, intense efforts are being dedicated to both understand the basic science underlying the pertinent materials as well to engineer higher energy density, improve safety, and prevent the progressive loss of capacity due to chemical and mechanical degradation [4–7]. Silicon is an important candidate material for anodes due to the potential of high specific charge capacity—more than ten times that of carbon-based materials [8]. However, during the charging and discharging processes, silicon electrodes experience remarkably large volumetric changes (as much as 300%, Fig. 1) and the concomitant stresses lead to nucleation of defects, and eventually, mechanical failure of the system [9]. As a result, the effective charge capacity often sharply reduces after just a few charging and discharging cycles [10–12].

The use of amorphous silicon (a-Si), instead of its crystalline counterpart, is considered to offer several advantages. Experiments have shown that the amorphous alloys tend to cycle better than the corresponding crystalline phases [13–15]. Crystalline Si, in fact, converts to amorphous Li-Si alloy phase during lithiation [16–18]. Finally, there is increasing evidence to indicate that the mechanical degradation of Si electrodes under electrochemical cycling may be mitigated by reducing their feature size, i.e., by using nanoscale configurations such as nanowires, nanoparticles among others [5,19]. Accordingly, this work is focused on understanding the atomistic mechanisms underpinning plasticity in a-Li-Si *nanostructures*.

Over the past decade or so, a variety of phenomenological (and increasingly sophisticated) continuum theories have been proposed to describe the elastic-plastic behavior of lithiated Si electrode [11,20,21]. For example, earlier work by Sastry [22] focused on using linearized elasticity and simple thermodynamic considerations for the stress analysis of lithiated electrodes, while subsequent ones have addressed fracture [23,24], the importance of large deformation and plasticity [20,25,26], rigorous continuum framework [27–29], proper consideration of the interplay between electrochemistry and mechanics [30], and design of optimal motifs [31] among others [32]. However, the atomistic and micromechanisms underpinning the observed plastic behavior of Li-Si alloys, to date, remains unclear.

In parallel and complementary to continuum models, empirical force-field based molecular dynamics (MD), as well as more fundamental approaches such as quantum-based density functional theory (DFT) calculations [33,34], have

*psharma@uh.edu

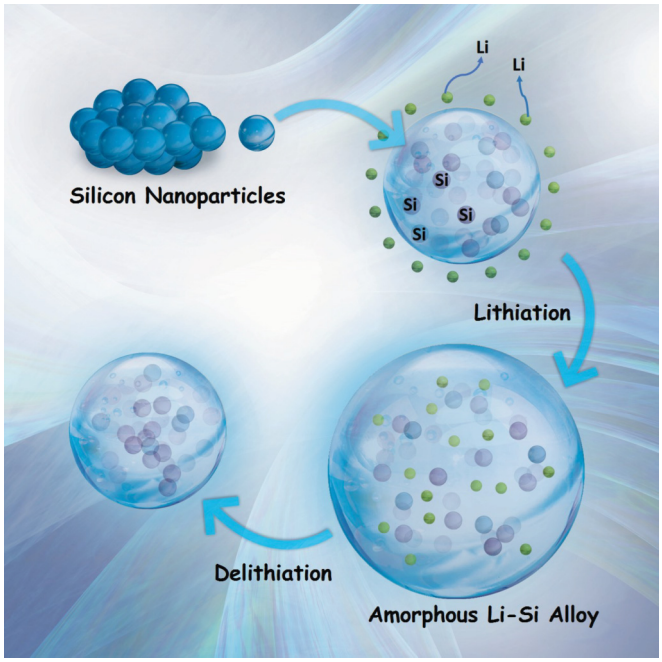

FIG. 1. Schematic of the lithiation and delithiation processes in Si nanoparticles. Lithiation dramatically enlarges the volume of the nanoparticle and alters the position of the host Si atoms. During delithiation, while some of the deformation is reversed (elastic deformation), the original microstructure is irreversibly altered (plastic deformation).

been used to obtain atomistic insights into the electro-chemical and mechanical behavior of lithium-ion battery materials—from electrodes [35,36] to electrolytes [37,38]. While these atomistic modeling works have provided interesting and valuable insights, there is a fundamental limitation of conventional MD methodology that precludes an assessment of material behavior over realistic laboratory-timescales. MD can only handle time scales of the order of, at best, a few microseconds. Even though this is adequate for understanding several physical, chemical, and mechanical phenomena in materials, the inability to address long-time scales prevents an assessment of slow-strain rate mechanical behavior that is the norm in laboratory experiments and real-life applications. We hardly need to emphasize that strain rate has a profound impact on the plastic deformation behavior of materials [39]. In this research, we employ a time-scaling atomistic approach to understand the fundamental mechanisms underpinning plasticity in amorphous fully lithiated nanostructures at room temperature. Our approach allows us to consider strain rates as low as 10^3 s^{-1}, which is several orders of magnitude beyond the reach of conventional molecular dynamics.

II. APPROACH

Our three-dimensional model system is depicted in Fig. 2, which is a fully lithiated amorphous silicon ($Li_{15}Si_4$) nanostructure at room temperature and consists of 4864 atoms. Fully lithiated silicon is the most severe case as far as mechanical deformation is concerned. The amorphous structure is created *via* a melting and quenching process. We

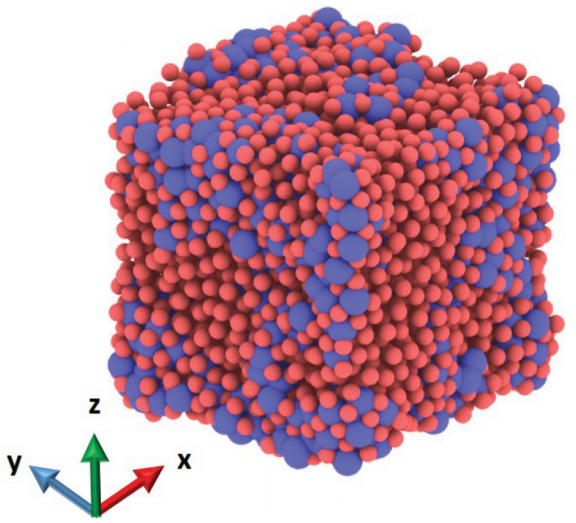

FIG. 2. Initial amorphous $Li_{15}Si_4$ alloy nanostructure. Red small balls represent Li atoms and large blue balls represent Si atoms.

increase the temperature of an initial crystalline structure to 4000 K, relax the structure for 1000 ps and decrease the temperature with the quenching rate of 3.7 K/ps to room temperature. An external pressure of 50 bar is applied during the annealing process. After the temperature is decreased to room temperature, the system is equilibrated using NPT (zero pressure) ensemble for another 1000 ps. The top and bottom layers are constrained to allow the application of a constant tensile strain rate in the z direction, while the lateral surfaces in x and y directions are kept free [40]. The modified embedded-atom method (MEAM) potential is used in all of the calculations presented in this work [41]. This potential has been widely used in the study of amorphous and crystalline Li-Si alloy and appears to provide a reasonable description of its mechanical properties [35,42,43].

We consider two imposed strain rates—the benchmark high strain rate of 10^8 s^{-1}, which is accessible with conventional MD and the low strain rate of 10^3 s^{-1}. We briefly summarize the approach used for time scaling. Since this approach has been described in detail elsewhere [43–48], including in a recent review article [49], we avoid an elaborate discussion regarding the method. In this approach, the desired strain rate ($\dot{\varepsilon}$) is first fixed and then the strain is imposed on the system in small incremental steps. The potential energy surface (PES) during each small strain increment is identified by using the so-called autonomous basin climbing (ABC) algorithm [44,50], which is implemented by us through an in-house code utilizing the LAMMPS software [51]. The ABC algorithm therefore yields as output the minima and saddle points of the PES (and therefore also the energy barriers between different local minima). The aforementioned PES sampling approach has been successfully applied in the study of the mechanical behavior of both crystalline [52] and amorphous systems [53,54]. The $3N$-dimensional PES is quite complex and the use of the ABC algorithm for even a few hundred atoms is computationally very demanding [44,55].

The energy barriers obtained from ABC are approximate since the determination of the saddle points can be in error

based on the resolution of the sampling approach. Accordingly, to extract accurate energy barriers, the nudged elastic band method (NEB) is applied to refine the barriers from the initial state to all possible final minima identified in the sampling process. With the energy barriers in hand, kinetic Monte Carlo (KMC) is used to find the most probable pathway based on the relative probability [56]. From the barrier energy of this selected transition, transition state theory is used to evaluate the time: $\Delta t = [\nu \exp(-\Delta E/k_b T)]^{-1}$, ν is the hopping frequency [57], T is temperature. Finally, the transition time multiplied by pre-defined strain rate ($\dot{\varepsilon}$) yields the strain increment for the next iteration through $\Delta\varepsilon = \dot{\varepsilon}\Delta t$. The calculated strain increment ($\Delta\varepsilon$) is applied to the system and a new round of ABC sampling, NEB, KMC (i.e., the entire aforementioned process) is repeated. In the recent review paper (mentioned earlier), a detailed comparison of the various ABC-based approaches has been made including how the one used in the present work (proposed by Fan *et al.* [58]) differs from what was outlined in the earlier papers [44,59,60].

III. RESULTS AND DISCUSSION

We first compare our time-scaling based simulation of high strain rate (10^8 s^{-1}) with MD results [Fig. 3(a)]. MD simulation is performed on the same structure initially equilibrated at 300 K, but deformed at a temperature close to zero under a strain rate of 10^8 s^{-1}. Seven independent MD simulation runs were carried out and the average stress-strain response is used for comparison. As evident, as far as this high strain rate case is concerned, ABC-based calculations and MD results are in *reasonable* accord [61]. For the high strain rate of 10^8 s^{-1}, the nanostructure appears to yield "roughly" around 1.0 GPa [62]. Based on this benchmark comparison, we conclude that the present time-scaling method can reasonably capture high strain rate deformation behavior of amorphous $Li_{15}Si_4$ nanostructures or, at least, agrees with conventional MD. We note that the yield stress for *bulk* Li-Si is less than 0.5 GPa [41].

We now turn to the key objective of this work imposition of low-strain rates that are inaccessible by conventional MD. The resulting stress-strain curves are shown in Fig. 3(b). The two different stress-strain curves correspond to the two tensile rates, 10^8 and 10^3 s^{-1}. We remark here that the simplicity of the results depicted in Fig. 3(b) is deceptive. For example, the MD result shown in Fig. 3 needs merely 20 hours (12 processors), while, the curve shown in Fig. 3(b) requires 4500 computational hours to obtain. Before we examine the mechanisms for plasticity, it is instructive to compare the emergent stress-strain behavior of the nanostructure plastic response for the two different strain rates. Not only is the yield strength highly rate dependent (as expected), the difference between the rates is quite significant; the high-strain rate yield stress is nearly 80% larger, which implies that conventional MD simulations are certainly inadequate to predict the key macroscopic parameter that dictates the plastic response of $Li_{15}Si_4$ nanostructure. The slow loading process that the time-scaling approach enables, allows longer time for structural relaxation and self-adjustment. As a result, the yielding occurs at lower stresses at slower strain rate. Plastic deformation, as deduced by merely examining the stress-strain

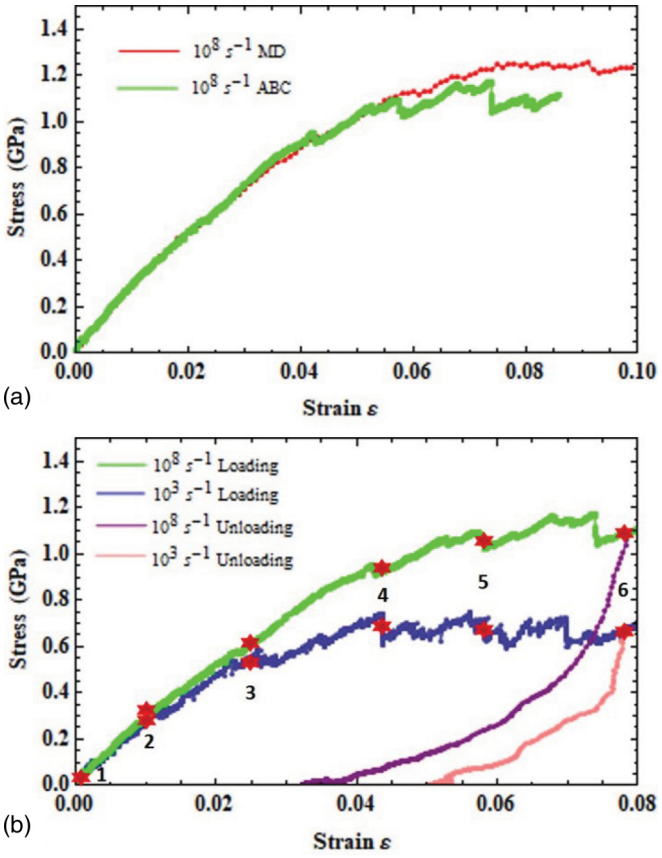

FIG. 3. (a) Stress-strain curves of the tensile test using averaged MD data (red curve) and the time-scaling approach (green curve) with imposed strain rate of 10^8 s^{-1}. (b) Stress-strain curves of loading and unloading for both slow and high strain rates. Red stars represent stages corresponding to (1) $\varepsilon = 0$, (2) 0.01, (3) 0.025, (4) 0.044, (5) 0.058, and (6) 0.079 and these snapshots are analyzed in detail in the main text.

curve, initiates much sooner at slow strain rate: at $\varepsilon = 0.025$ for slow strain rate and at $\varepsilon = 0.044$ for the faster strain rate. We also note the higher frequency of the stress drops (signifying microscopic dissipation events) during the slow loading process. It is also of interest to examine how different the rate behavior is as far as accumulated plastic strain is concerned—once the load is removed. For both the slow and fast rates, we unload from the strain value of $\varepsilon = 0.079$. The residual plastic strain, after complete unloading, is 0.032 for the high strain rate case and 0.05 for the low strain rate case—again, a rather significant difference. Further discussion regarding the unloading behavior may be found in Appendix.

We now turn to an investigation into the atomistic mechanisms that lead to the emergent plasticity behavior shown in Fig. 3(b). To quantify the plastic deformation at the atomic level, we use the approach laid out in Refs. [63,64] to study amorphous systems. For that, two quantities—the local shear strain (η_i^s) and nonaffine squared displacement ($D^2_{\min}$)—are evaluated. The index i labels the atom. Evaluation of η_i^s requires two configurations, the reference one and the current one. To facilitate a subsequent comparison between the two loading rates, we take the initial configuration as the reference [corresponding to label 1 in Fig. 3(b)] and all the labeled

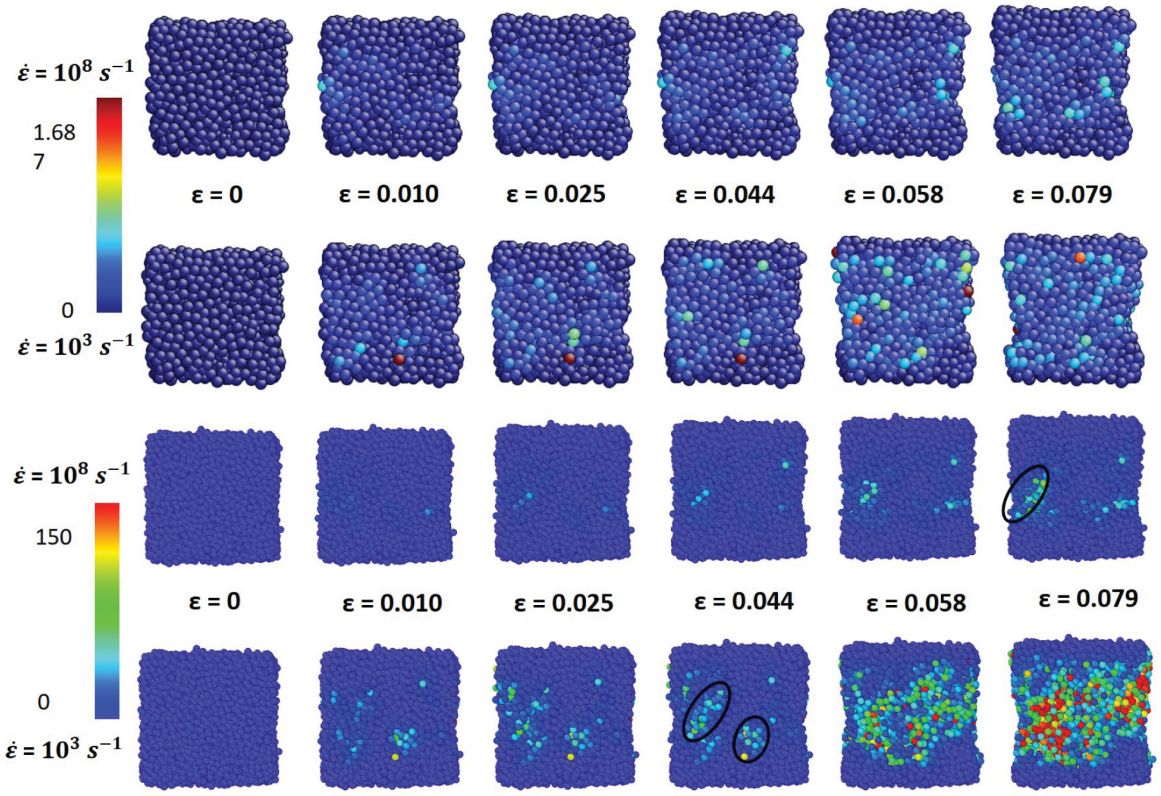

FIG. 4. (a) Local shear strain (η_i^s) visualization of high strain rate case (top row) and the low strain rate case (bottom row) corresponding to different strain values. (b) Nonaffine squared displacement visualization of {010} free surface for the high strain rate case (top row) and low strain rate case (bottom row) for different strain values. Black circles highlight a few examples of shear transformation zones.

points as "current" configurations corresponding to different strain values. The local Lagrangian strain matrix $\boldsymbol{\eta}_i$ can then be calculated from

$$\boldsymbol{\eta}_i = \tfrac{1}{2}\left(\boldsymbol{J}_i^T \boldsymbol{J}_i - \boldsymbol{I}\right), \tag{1}$$

where $\boldsymbol{I}$ is identity matrix and $\boldsymbol{J}_i$ is an affine transformation matrix, which transforms the initial configuration to the current configuration. The dilatational component is

$$\eta_m = \tfrac{1}{3}\mathrm{Tr}(\boldsymbol{\eta}_i), \tag{2}$$

and the scalar measure of the local shear strain content η_i^s is defined as

$$\eta_i^s = \sqrt{\frac{1}{2} Tr(\boldsymbol{\eta}_i - \eta^m \boldsymbol{I})^2}. \tag{3}$$

As shown in Fig. 4(a), with the increase of the applied strain, both the high strain rate and low strain rate cases exhibit increasing local shear strain. Comparison between top row (high strain rate) and bottom row (low strain rate) in Fig. 4(a) reveals that atoms with higher shear strain under high strain rate loading are localized at the center of the nanostructure, while the high shear strained in the low strain rate case are more evenly distributed in the specimen ($\varepsilon = 0.058$ and 0.079). In other words, more localization becomes evident under high strain rates.

To systematically analyze the plastic deformation and identify the exact region where the irreversible plastic rearrangements are occurring—the so-called shear transformation zones (STZs) [65] need to be identified. The concept of STZ's has been extensively invoked in the study of plasticity of amorphous materials (see, for example, Ref. [66] and references therein). Besides analyzing local shear strain, which represents the shear content of the multiaxial deformation field correspond to an affine shape change, nonaffine squared displacement (D^2_{min}) is calculated to pinpoint the location of the STZs [64,65]. Similar to local shear strain, the calculation of nonaffine squared displacement also require two configurations. We take the initial structure as the reference configuration and all the labeled points in Fig. 3(b) as current configurations. First, we apply an affine transformation to the distance vector between neighboring particle (j) within the cutoff distance r_c (assume there are N_i atoms within r_c and $j \in N_i$) and the center particle (i) at reference time [63,64]

$$\boldsymbol{r}^a_{ji}(0) = \boldsymbol{J}_i \boldsymbol{r}_{ji}(0), \tag{4}$$

where the distance vector $\boldsymbol{r}_{ji}(0)$ is defined as

$$\boldsymbol{r}_{ji}(0) = \boldsymbol{r}_j(0) - \boldsymbol{r}_i(0). \tag{5}$$

Analogous to the way mean square displacement (MSD) is defined, D^2 for each single atom can be expressed as

$$D^2 = \frac{1}{N_i} \sum_{j \in N_i} \left[\boldsymbol{r}_{ji}(t) - \boldsymbol{r}^a_{ji}(0)\right]^2. \tag{6}$$

The difference between MSD and D^2 is that MSD ($\mathrm{MSD} = \frac{1}{N}\sum_{n=1}^{N} [\boldsymbol{x}(t) - \boldsymbol{x}(0)]^2$) is an evaluation based on

atom position vectors $\boldsymbol{x}$, while D^2 is a measure of the nonafffine deformation content. From Eqs. (6) and (4), D^2 depends on both distance vectors as well as affine matrix $\boldsymbol{J}_i$. To minimize the error of deformation mapping, the best affine transformation matrix need to be used and the nonaffine squared displacement $D^2_{\min}$ is defined as [63,64]

$$D^2_{\min} = \frac{1}{N_i} \min_{\boldsymbol{J}_i} \sum_{j \in N_i} \left[\boldsymbol{r}_{ji}(t) - \boldsymbol{r}^a_{ji}(0) \right]^2. \tag{7}$$

The results for the computed nonaffine squared displacement for the labeled points in Fig. 3(b) on the $\{010\}$ surface are shown in Fig. 4(b). The top row constitutes the snapshots for the high strain rate case and the bottom row contains the snapshots for the low strain rate case. The nucleation of STZs [black circles in Fig. 4(b)] is shown for both cases. The low strain rate loading process nucleates STZs at an earlier stage compared to high strain rate loading. The STZs can be observed at the strain of 0.025 or even earlier during slower loading while they appear around $\varepsilon = 0.058$ in high strain rate situation. Furthermore, the size of STZs in the low strain rate case is larger than for the high strain rate case and the latter exhibit higher values of $D^2_{\min}$ (atoms in red color). Comparison of the snapshots shown in Figs. 4(a) and 4(b) reveals that the larger values of η^s_i appear in the same region as the larger values of $D^2_{\min}$. The correlated relation of η^s_i and $D^2_{\min}$ is because the plastic deformation from shape change (represented by η^s_i) will introduce local particle rearrangement in the neighborhood (represented by $D^2_{\min}$). Massive atomistic rearrangement is notable for slow strain rate case—which allows neighboring atoms the sufficient time and "luxury" to rearrange themselves. These self-rearrangements can involve the participation of more neighboring atoms and generate denser STZs with higher $D^2_{\min}$ values.

Theoretical models reported in Refs. [67–69] indicate that for a strained amorphous solid, it is energetically favorable to have localized nonaffine plastic flow in a shear band which lies at 45° to the principal stress axis (loading direction of uniaxial tension). We attempt to visualize this interesting phenomenon from an atomistic viewpoint using our simulation results, thus we focus on $\{110\}$ section, which is parallel to the loading direction (Fig. 5). We find that the atoms with high $D^2_{\min}$ lie along lines (black lines) which are roughly 45° with the loading direction (z direction shown in red arrows). While the theoretical predictions are for a bulk system, it is interesting to note that even for a nanostrucutre, the shear band orientation is close to the predicted value of 45°.

As it is well known, dislocations are the microscopic plasticity carriers for crystalline materials, however, for amorphous system, the unit plasticity events have been a matter of much debate—see Ref. [70] and references therein. While we certainly cannot resolve that issue in this work, we hope to critically examine the deformation in the STZs of LiSi nanostructure to see if we can ascertain the major dissipative mechanisms. In order to better visualize the evolution of STZs we focus on the $\{1\bar{1}0\}$ section, which is also parallel to the loading direction (Fig. 6). On this surface, the effect of maximum shear stress (in principle, along the directions having 45° angle with the loading direction) on STZs should be most relevant. In Fig. 6, clear differences between the high

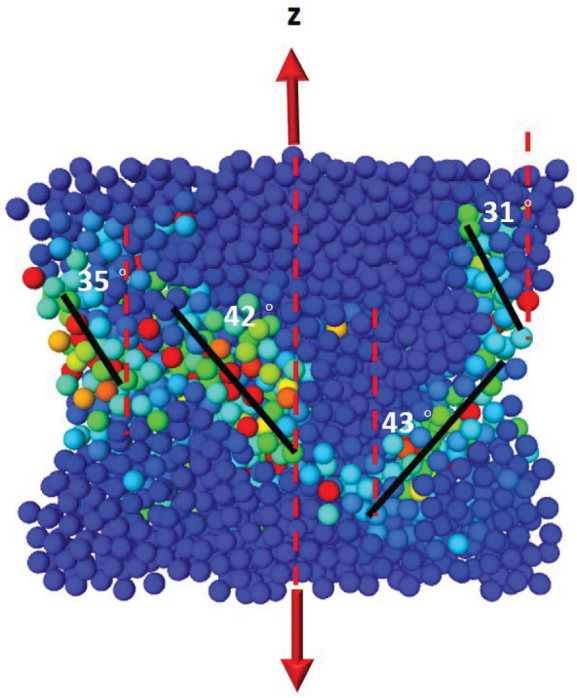

FIG. 5. Snapshot for $\{110\}$ surface of low strain rate case with $\varepsilon = 0.079$. Atoms are colored according to their values of $D^2_{\min}$ using the same scale as in Fig. 4(b). Red arrows represent the loading direction and black lines represent the "shear bands."

strain rate case (top row) and the low strain rate case (bottom row) are observed on this section. At every strain value, except $\varepsilon = 0$, STZs in the low strain rate case are larger in size and exhibit a higher value of $D^2_{\min}$ compared with the STZs under high strain rate snapshots. We also note that STZs appear in similar regions across both fast and slow rate cases. The snapshots at $\varepsilon = 0.079$ are good examples of this observation. For the low strain rate case, the STZs (circled in black) are formed with very high $D^2_{\min}$ (atoms with red color), while in the same region for sample loading with low strain rate, less dense STZs with lower $D^2_{\min}$ appear. Regardless of the strain rate, local atomic re-arrangements or microadjustments appear to be the key stress-accommodation process. However, in the case of fast loading, there is not enough "time" for the atoms to dissipate energy and the corresponding stress-strain curve (green) shown in Fig. 3(b) is smoother with only a few drops. Slow loading process, however, allows the neighboring atoms to adjust themselves corresponding to the shape change so that the stresses on the atoms are relieved much more efficiently. Due to the longer relaxation time, frequent energy dissipation events yield multiple successive bursts evident in the blue curve of Fig. 3(b).

In the charging and discharging process, Li ions migrate from one electrode *via* the intervening electrolyte and insert and diffuse in the opposite electrode. The insertion and diffusion of Li ions is accompanied by a rather large volumetric swelling and the consequent generation of mechanical stresses. Li and Si play different roles in the battery system. Thus it is worthwhile to assess the behavior and contribution of these two types of atoms to the plastic deformation of the alloy.

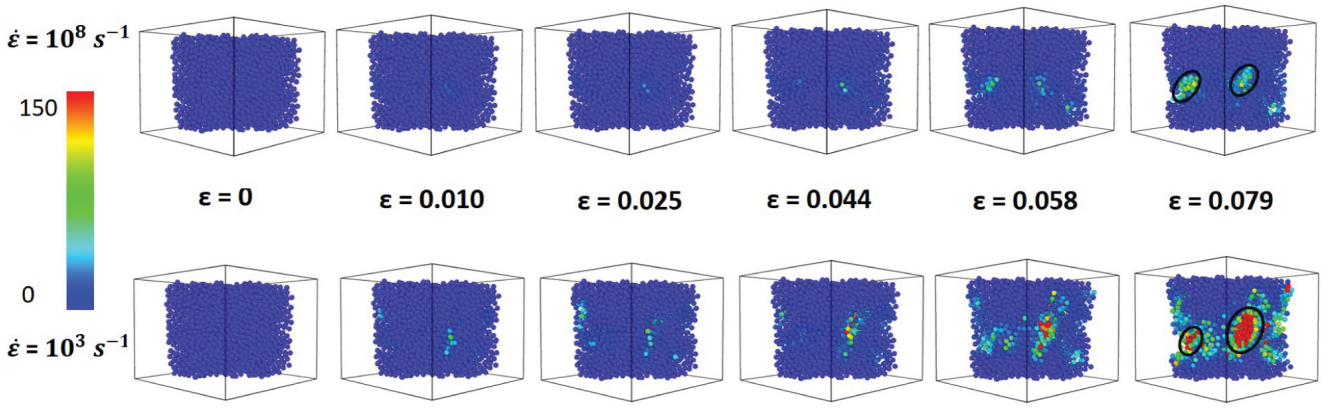

FIG. 6. Nonaffine squared displacement visualization of $\{1\bar{1}0\}$ surface with high strain rate stretching (top row) and low strain rate stretching (bottom row) at different strain values. Black circles highlight two examples of STZs.

As shown in Fig. 7, we plot the distributions of nonaffine squared displacement ($D^2_{\min}$) of Li and Si separately. In this figure, the horizontal axis is the value of nonaffine squared displacement and the vertical axis represents the corresponding number of atoms. The distribution of Li atoms is shown in blue and the distribution of Si atoms is shown in purple. The inset (the zoomed-in view of the red dashed box) shows the distribution and numbers of atoms with higher value of $D^2_{\min}$ (red atoms in Figs. 4 and 6). We note that for higher values of $D^2_{\min}$ ($D^2_{\min} > 50$), the ratio between the number of Li atoms and Si atoms is much higher than the average atom ratio (the average ratio is 3.75 for $Li_{15}Si_4$). On the other hand, the ratio between Li atoms and Si atoms is lower than 3.75 for lower values of $D^2_{\min}$ (3.05 for the first bar in Fig. 7, which represents $D^2_{\min} < 50$). This observation, in our opinion, signifies that Li is more active in the plastic deformation. In other words, more Li atoms, compared with Si atoms play the role of plasticity carriers. Interesting, a similar conclusion was reached in Ref. [71] using an entirely different approach where they argue that Si forms the skeleton of the structure and the Li atoms are the "flowing defects" of the system.

To further understand what happens during slow strain rate deformation, we also tracked the movement of a group of atoms in a STZ during the deformation process. As shown in Fig. 8, we track the atoms inside of the STZs shown in Fig. 6 (snapshot of slow strain rate case at $\varepsilon = 0.079$). Figures 8(a) and 8(b) illustrate deformation which mainly occurs in elastic regime [points 1 and 3 in Fig. 3(b)]. Here there is no significant variation of the relative positions (colored atoms in ellipsoid). With the larger amount of deformation [$\Delta\varepsilon = 0.035$ from Figs. 8(c) to 8(d) and $\Delta\varepsilon = 0.025$ from Figs. 8(a) to 8(b)], in the plastic deformation region [points 4 and 6 in Fig. 3(b)], the STZ in Fig. 8(c) rotates clockwise and becomes the shape shown in Fig. 8(d). Additional rotation also occurs in the out-of-plane direction, however we don't emphasize this part because it shares the same physics as

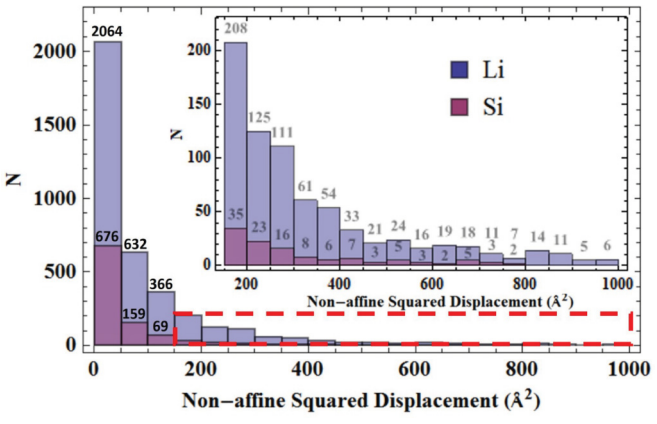

FIG. 7. Nonaffine squared displacement of Li and Si atoms. The subset (a zoomed view of red dashed box) shows the distribution and numbers of atoms for both Li and Si atoms at higher value of $D^2_{\min}$.

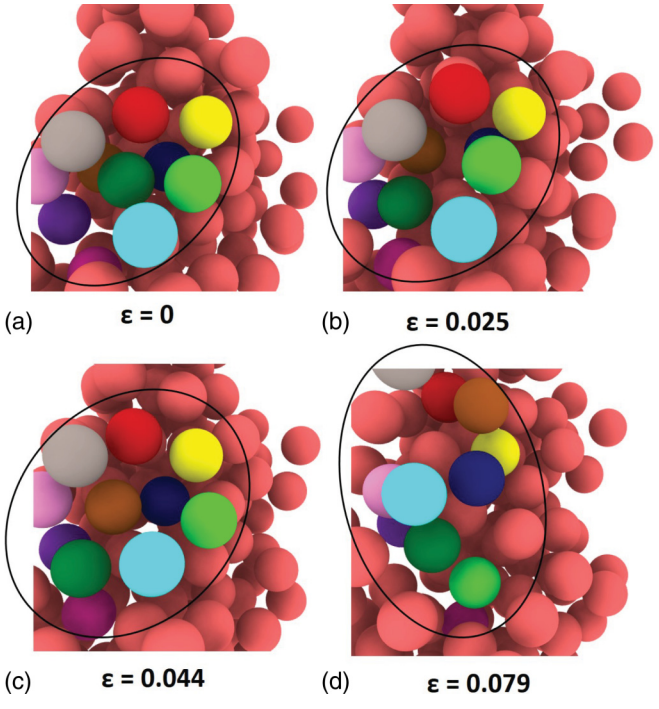

FIG. 8. Tracing map of the positions of a few atoms (in different colors) inside the big STZ in the snapshot of low strain rate case at $\varepsilon = 0.079$ in Fig. 6. The snapshots are taken at (a) $\varepsilon = 0$, (b) $\varepsilon = 0.025$, (c) $\varepsilon = 0.044$, and (d) $\varepsilon = 0.079$.

what we observed from Fig. 8. This type of rotation is in our opinion an important dissipation mechanism for plasticity in LiSi amorphous nanostructures. During elastic deformation, because of stretching, atoms are subjected to increasing stress. Correspondingly, in Fig. 3(b), the stress difference between point 1 and 3 is 0.5 GPa. For plastic deformation, due to the aforementioned relative rotation of a group of atoms, with larger amount of strain increment, the stresses at points 4 and 6 in Fig. 3(b) are almost the same.

IV. SUMMARY

In summary, with the help of a time-scaling atomistic simulation approach, we have provided insights into the key atomistic mechanisms underpinning plasticity in lithium-silicon nanostructures. Due to its inability to handle lower strain rates, conventional molecular dynamics overestimates the yield stress, underestimate the accumulated plastic strain and misses important microscopic events underlying the plasticity response of LiSi. In this research, we were able to simulate a slow strain rate to 10^3 s^{-1} and compared the atomistic behavior with the system under high strain rate loading. Our simulations show reduced yield stress for slow loading process with more frequent dissipation events in comparison with the high strain rate loading process. Direct atomistic visualization reveal a plethora of insights into the microscopic dissipation processes underlying plastic deformation and we conclude that rotation of localized regions in the shear transformation zones is likely an important dissipation mechanism for amorphous Li-Si alloy.

ACKNOWLEDGMENTS

We gratefully acknowledge partial support from the M.D. Anderson Professorship and NSF CMMI grant No. 1463205. PRG acknowledges support from the United States Department of Energy EPSCoR Implementation award (Grant No. DE-SC0007074).

APPENDIX: ATOMISTIC ANALYSIS OF UNLOADING

During the unloading process, the constraints are removed from the system and the system undergoes a recovery process. From Fig. 2(b), as evident, the unloading process is not linear. We first visualize the nonaffine squared displacement ($D^2_{\min}$) on the $\{1\bar{1}0\}$ surface (Fig. 9). In general, the length in z direction (loading direction) is reduced. Comparison between the snapshots before and after unloading for both high strain rate loading process and low strain rate loading process reveals that the shape and location of the shear transformation zones (STZs) remain unaltered.

The zoomed-in view of the STZs are shown in Fig. 10. In the top row of this figure, colored atoms are selected from the black circle shown in Fig. 9(b). Figures 10(a) and 10(b) demonstrate the elastic recovery—reduction of the distance between atoms. Similar (less significant) observations can be found in the snapshots in the bottom row [Figs. 10(c) and 10(d)] and they display the tracked atoms for the unloading process in the slow strain rate deformation case. The colored atoms are the same as Fig. 6.

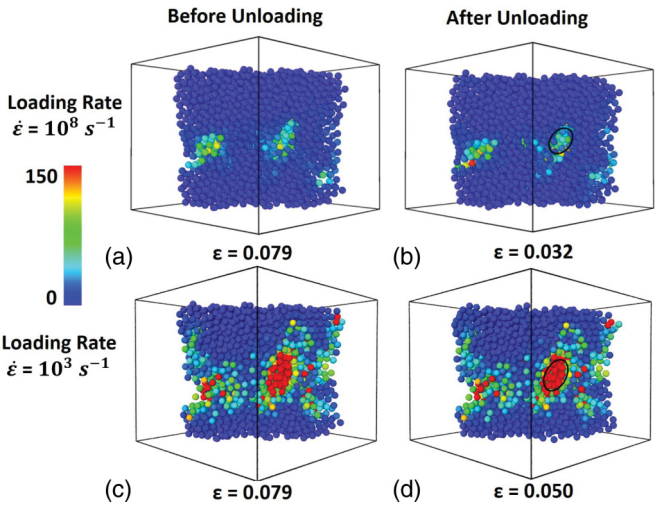

FIG. 9. Nonaffine squared displacement visualization of $\{1\bar{1}0\}$ surface with snapshots of (a) before unloading from high strain rate deformation, (b) after unloading from high strain rate deformation, (c) before unloading from low strain rate deformation, and (d) after unloading from low strain rate deformation. The reference configuration is the initial configuration before loading ($\varepsilon = 0$).

From the unloading curves in Fig. 3, reverse plastic deformation also occurs during the unloading process. However, this is difficult to observe from the atomistic snapshots in Figs. 9 and 10. To facilitate a quantitative evaluation of the reverse plastic deformation, we calculate nonaffine squared displacement with the configuration before unloading as the reference configuration and the results are shown in Fig. 11. In the snapshot for high strain rate loading process [Fig. 11(a)], the zone of the reverse plastic deformation is in the center of the system. We remark that different coloring

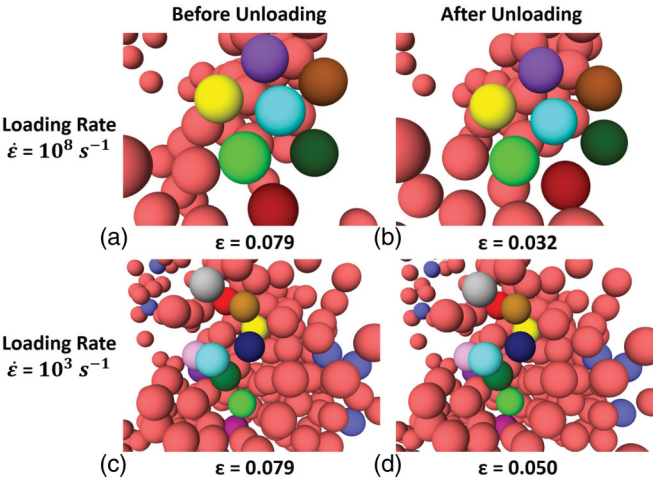

FIG. 10. Tracking map of the positions of a few atoms (rendered in different color) inside the STZ. The snapshots of (a) before unloading from high strain rate deformation, (b) after unloading from high strain rate deformation, (c) before unloading from low strain rate deformation, and (d) after unloading from low strain rate deformation. Colored atoms for low strain rate case [(c) and (d)] are same as the ones in Fig. 6.

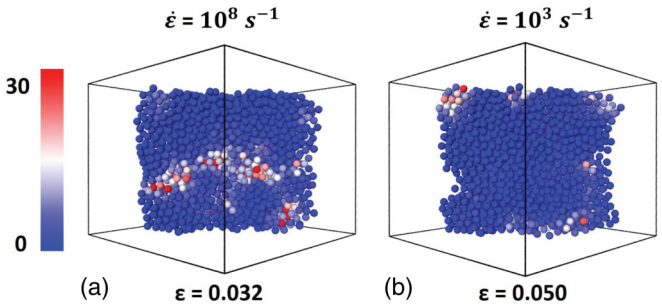

FIG. 11. Nonaffine squared displacement visualization of $\{1\bar{1}0\}$ surface with snapshots of unloading from high strain rate deformation (left) and low strain rate deformation (right). The reference configuration is the one before unloading ($\varepsilon = 0.079$).

system is adapted in this figure from Figs. 4 and 6 since the value of $D^2_{\min}$ is much smaller as compared to the loading process. As shown in Fig. 3(b), during unloading (for the high strain rate case), roughly 0.01 plastic strain is reversed (there is 0.04 plastic strain accumulated in loading process for high strain rate loading case). Thus we adjusted the coloring scale to yield better visualization. The reverse plastic deformation for low strain rate deformation is even smaller (0.005) and the distribution of $D^2_{\min}$ is shown in Fig. 11(b). Such difference between unloading process for high strain rate and low strain rate deformation is due to fact that the self-rearrangement is irreversible and atoms are "locked" after this type of self-adjustments. For the slow loading process, more atoms are involved in this irreversible rearrangement and the plastic deformation accumulated during loading remains even after unloading. We speculate that for the high strain rate loading process, atoms are unable to access entropically favorable states and there is therefore more scope for reverse plastic deformation can happen in the unloading process.

[1] B. Kang and G. Ceder, Nature (London) **458**, 190 (2009).
[2] C. K. Chan, X. F. Zhang, and Y. Cui, Nano Lett. **8**, 307 (2008).
[3] B. Moradi and G. G. Botte, J. Appl. Electrochem. **46**, 123 (2016).
[4] M. Winter and J. O. Besenhard, Electrochim. Acta **45**, 31 (1999).
[5] X. H. Liu, L. Zhong, S. Huang, S. X. Mao, T. Zhu, and J. Y. Huang, ACS Nano **6**, 1522 (2012).
[6] U. Kasavajjula, C. Wang, and A. J. Appleby, J. Power Sources **163**, 1003 (2007).
[7] T. Kelly, B. M. Ghadi, S. Berg, and H. Ardebili, Sci. Rep. **6**, 20128 (2016).
[8] J.-M. Tarascon and M. Armand, Nature (London) **414**, 359 (2001).
[9] X. H. Liu, H. Zheng, L. Zhong, S. Huang, K. Karki, L. Q. Zhang, Y. Liu, A. Kushima, W. T. Liang, J. W. Wang *et al.*, Nano Lett. **11**, 3312 (2011).
[10] J. Maranchi, A. Hepp, A. Evans, N. Nuhfer, and P. Kumta, J. Electrochem. Soc. **153**, A1246 (2006).
[11] H. B. Chew, B. Hou, X. Wang, and S. Xia, Int. J. Solids Struct. **51**, 4176 (2014).
[12] H. Wang, B. Hou, X. Wang, S. Xia, and H. B. Chew, Nano Lett. **15**, 1716 (2015).
[13] L. Beaulieu, K. Eberman, R. Turner, L. Krause, and J. Dahn, Electrochem. Solid-State Lett. **4**, A137 (2001).
[14] L. Beaulieu, K. Hewitt, R. Turner, A. Bonakdarpour, A. Abdo, L. Christensen, K. Eberman, L. Krause, and J. Dahn, J. Electrochem. Soc. **150**, A149 (2003).
[15] L. Beaulieu, T. Hatchard, A. Bonakdarpour, M. Fleischauer, and J. Dahn, J. Electrochem. Soc. **150**, A1457 (2003).
[16] P. Limthongkul, Y.-I. Jang, N. J. Dudney, and Y.-M. Chiang, Acta Mater. **51**, 1103 (2003).
[17] P. Limthongkul, Y.-I. Jang, N. J. Dudney, and Y.-M. Chiang, J. Power Sources **119-121**, 604 (2003).
[18] C. K. Chan, H. Peng, G. Liu, K. McIlwrath, X. F. Zhang, R. A. Huggins, and Y. Cui, Nat. Nanotechnol. **3**, 31 (2007).
[19] S. W. Lee, M. T. McDowell, L. A. Berla, W. D. Nix, and Y. Cui, Proc. Nat. Acad. Sci. USA **109**, 4080 (2012).
[20] A. F. Bower, P. R. Guduru, and V. A. Sethuraman, J. Mech. Phys. Solids **59**, 804 (2011).
[21] L. Brassart and Z. Suo, J. Mech. Phys. Solids **61**, 61 (2013).
[22] X. Zhang, W. Shyy, and A. M. Sastry, J. Electrochem. Soc. **154**, A910 (2007).
[23] K. Zhao, M. Pharr, J. J. Vlassak, and Z. Suo, J. Appl. Phys. **108**, 073517 (2010).
[24] K. Zhao, M. Pharr, L. Hartle, J. J. Vlassak, and Z. Suo, J. Power Sources **218**, 6 (2012).
[25] K. Zhao, M. Pharr, S. Cai, J. J. Vlassak, and Z. Suo, J. Am. Ceram. Soc. **94**, s226 (2011).
[26] L. Anand, J. Mech. Phys. Solids **60**, 1983 (2012).
[27] C. V. Di Leo, E. Rejovitzky, and L. Anand, Int. J. Solids Struct. **67-68**, 283 (2015).
[28] S. W. Lee, H.-W. Lee, I. Ryu, W. D. Nix, H. Gao, and Y. Cui, Nat. Commun. **6**, 7533 (2015).
[29] C. V. Di Leo, E. Rejovitzky, and L. Anand, J. Mech. Phys. Solids **70**, 1 (2014).
[30] Y. Li, F. El Gabaly, T. R. Ferguson, R. B. Smith, N. C. Bartelt, J. D. Sugar, K. R. Fenton, D. A. Cogswell, A. D. Kilcoyne, T. Tyliszczak *et al.*, Nat. Mater. **13**, 1149 (2014).
[31] J. L. Goldman, B. R. Long, A. A. Gewirth, and R. G. Nuzzo, Adv. Funct. Mater. **21**, 2412 (2011).
[32] For the sake of brevity, we avoid a detailed survey of the rather vast literature on the continuum mechanics work on this topic. The reader is referred to the following review article and references therein [72].
[33] J. W. Wang, Y. He, F. Fan, X. H. Liu, S. Xia, Y. Liu, C. T. Harris, H. Li, J. Y. Huang, S. X. Mao *et al.*, Nano Lett. **13**, 709 (2013).
[34] K. Zhao, W. L. Wang, J. Gregoire, M. Pharr, Z. Suo, J. J. Vlassak, and E. Kaxiras, Nano Lett. **11**, 2962 (2011).
[35] H. Wang, X. Wang, S. Xia, and H. B. Chew, J. Chem. Phys. **143**, 104703 (2015).
[36] H. Wang and H. B. Chew, Extreme Mech. Lett. **9**, 503 (2016).
[37] S.-P. Kim, A. C. Van Duin, and V. B. Shenoy, J. Power Sources **196**, 8590 (2011).

[38] Q. Li and H. Ardebili, Solid State Ionics **268**, 156 (2014).
[39] D. Hell and D. J. Bacon, *Introduction to Dislocations*, 5th ed. (Elsevier, Kidlington, Oxford, 2011).
[40] We remark here that the goal of the current work is *not* to simulate an actual battery operation. In fact, that would be very difficult to do completely in an atomistic context. Our key motivation is that the actual micromechanisms of plasticity at the material level (for Si-Li) are not understood—whether the stresses originate from an actually externally applied stress or via lithiation. Therefore we do not directly address battery operational processes and the central objective of the work is the elucidation of basic physics/science underpinning the mechanical behavior at the material level. In a battery, cycling of Si anodes (most likely in the form of Si particles) involves more complicated lithiation conditions and stress states, but the analysis and elucidation of such complex states can be build upon an understanding of the simpler and controlled stress and deformation states such as the uniaxial loading considered here. Results from such simpler numerical experiments can be used to develop general (continuum) models that can be applied to real-life complex states.
[41] Z. Cui, F. Gao, Z. Cui, and J. Qu, J. Power Sources **207**, 150 (2012).
[42] B. Ding, X. Li, X. Zhang, H. Wu, Z. Xu, and H. Gao, Nano Energy **18**, 89 (2015).
[43] X. Yan, A. Gouissem, and P. Sharma, Mech. Mater. **91**, 306 (2015).
[44] A. Kushima, X. Lin, J. Li, J. Eapen, J. C. Mauro, X. Qian, P. Diep, and S. Yip, J. Chem. Phys. **130**, 224504 (2009).
[45] Y. Fan, A. Kushima, S. Yip, and B. Yildiz, Phys. Rev. Lett. **106**, 125501 (2011).
[46] Y. Fan, A. Kushima, and B. Yildiz, Phys. Rev. B **81**, 104102 (2010).
[47] Y. Fan, Y. N. Osetsky, S. Yip, and B. Yildiz, Phys. Rev. Lett. **109**, 135503 (2012).
[48] X. Yan and P. Sharma, Nano Lett. **16**, 3487 (2016).
[49] X. Yan, P. Cao, W. Tao, P. Sharma, and H. S. Park, J. Phys. D **49**, 493002 (2016).
[50] A. Kushima, X. Lin, J. Li, X. Qian, J. Eapen, J. C. Mauro, P. Diep, and S. Yip, J. Chem. Phys. **131**, 164505 (2009).
[51] S. Plimpton, J. Comput. Phys. **117**, 1 (1995).
[52] X.-Z. Tang, Y.-F. Guo, Y. Fan, S. Yip, and B. Yildiz, Acta Mater. **105**, 147 (2016).
[53] P. Cao, M. Li, R. J. Heugle, H. S. Park, and X. Lin, Phys. Rev. E **86**, 016710 (2012).
[54] P. Cao, X. Lin, and H. S. Park, J. Mech. Phys. Solids **68**, 239 (2014).
[55] P. Cao, H. S. Park, and X. Lin, Phys. Rev. E **88**, 042404 (2013).
[56] A. F. Voter, in *Radiation Effects in Solids* (Springer, Dordrecht, 2007), pp. 1–23.
[57] We have used a hopping rate of $10^{13}\,s^{-1}$. Given the current strain-rate controlled loading scheme we use, the precise value is not too critical as long as the order of magnitude is reasonable. Rigorously speaking, this value must be computed for each transition and requires the calculation of normal modes for each saddle point; however a common approximation, for computational expediency, is to choose a fixed value within the typical range of 10^{12}–$10^{13}\,s^{-1}$, cf. Refs. [56,73].
[58] Y. Fan, Y. N. Osetskiy, S. Yip, and B. Yildiz, Proc. Nat. Acad. Sci. USA **110**, 17756 (2013).
[59] T. T. Lau, A. Kushima, and S. Yip, Phys. Rev. Lett. **104**, 175501 (2010).
[60] A. Kushima, J. Eapen, J. Li, S. Yip, and T. Zhu, Eur. Phys. J. B **82**, 271 (2011).
[61] The MD predictions do not match the ABC curve (green) *exactly*, however, the physical trend is the same. We note that for the high strain rate case, multiple MD simulations reveal that the yield stress varies between 1.1 and 1.4 GPa.
[62] Here we are using the word "yield" to signify the stress at which there is a marked departure from a linear stress-strain relation.
[63] F. Shimizu, S. Ogata, and J. Li, Mater. Trans. **48**, 2923 (2007).
[64] W. Li, J. M. Rieser, A. J. Liu, D. J. Durian, and J. Li, Phys. Rev. E **91**, 062212 (2015).
[65] M. Falk and J. Langer, Phys. Rev. E **57**, 7192 (1998).
[66] J. Langer, Phys. Rev. E **77**, 021502 (2008).
[67] R. Dasgupta, H. G. E. Hentschel, and I. Procaccia, Phys. Rev. Lett. **109**, 255502 (2012).
[68] R. Dasgupta, H. G. E. Hentschel, and I. Procaccia, Phys. Rev. E **87**, 022810 (2013).
[69] J. Ashwin, O. Gendelman, I. Procaccia, and C. Shor, Phys. Rev. E **88**, 022310 (2013).
[70] M. J. Demkowicz and A. S. Argon, Phys. Rev. B **72**, 245205 (2005).
[71] K.-J. Zhao, Y.-G. Li, and L. Brassart, Acta Mechanica Sinica **29**, 379 (2013).
[72] Y. Gao, M. Cho, and M. Zhou, J. Mech. Sci. Technol. **27**, 1205 (2013).
[73] L. Nguyen, K. Baker, and D. Warner, Phys. Rev. B **84**, 024118 (2011).